

Instability of a viscous interface under horizontal oscillation

Emma Talib and Anne Juel

Citation: *Phys. Fluids* **19**, 092102 (2007); doi: 10.1063/1.2762255

View online: <http://dx.doi.org/10.1063/1.2762255>

View Table of Contents: <http://pof.aip.org/resource/1/PHFLE6/v19/i9>

Published by the [American Institute of Physics](#).

Related Articles

Control of the antisymmetric mode ($m=1$) for high Reynolds axisymmetric turbulent separating/reattaching flows
Phys. Fluids **23**, 095102 (2011)

Spectral modeling of rotating turbulent flows
Phys. Fluids **22**, 025104 (2010)

Traveling-wave solutions of the flow in a curved-square duct
Phys. Fluids **20**, 124101 (2008)

A three-dimensional spectral boundary element algorithm for interfacial dynamics in Stokes flow
Phys. Fluids **18**, 082106 (2006)

Rossiter's formula: A simple spectral model for a complex amplitude modulation process?
Phys. Fluids **18**, 071703 (2006)

Additional information on Phys. Fluids

Journal Homepage: <http://pof.aip.org/>

Journal Information: http://pof.aip.org/about/about_the_journal

Top downloads: http://pof.aip.org/features/most_downloaded

Information for Authors: <http://pof.aip.org/authors>

ADVERTISEMENT



**Running in Circles Looking
for the Best Science Job?**

Search hundreds of exciting
new jobs each month!

<http://careers.physicstoday.org/jobs>

physicstodayJOBS



Instability of a viscous interface under horizontal oscillation

Emma Talib and Anne Juel^{a)}

Manchester Centre for Nonlinear Dynamics and School of Mathematics, The University of Manchester, Oxford Road, Manchester M13 9PL, United Kingdom

(Received 1 January 2007; accepted 22 June 2007; published online 18 September 2007)

The linear stability of superposed layers of viscous, immiscible fluids of different densities subject to horizontal oscillations, is analyzed with a spectral collocation method and Floquet theory. We focus on counterflowing layers, which arise when the horizontal volume-flux is conserved, resulting in a streamwise pressure gradient. This model has been shown to accurately predict the onset of the frozen wave observed experimentally [E. Talib, S. V. Jalikop, and A. Juel, *J. Fluid Mech.* **584**, 45 (2007)]. The numerical method enables us to gain new insights into the Kelvin–Helmholtz (KH) mode usually associated with the frozen wave, and the harmonic modes of the parametric-resonant instability, by resolving the flow for an exhaustive range of vibrational to viscous forces ratios and viscosity contrasts. We show that the viscous model is essential to accurately predict the onset of each mode of instability. We characterize the evolution of the neutral curves from the multiple modes of the parametric-resonant instability to the single frozen wave mode encountered in the limit of practical flows. We find that either the KH or the first resonant mode may persist when the fluid parameters are varied toward this limit. Interestingly, these two modes exhibit opposite dependencies on the viscosity contrast, which are understood by examining the eigenmodes near the interface. © 2007 American Institute of Physics. [DOI: 10.1063/1.2762255]

I. INTRODUCTION

The periodic excitation of fluid interfaces can lead to a wide variety of dynamics. Vertical oscillations, for instance, may either destabilize or restabilize fluid interfaces. Faraday waves are commonly observed at the interface between stably stratified fluids,¹ while the Rayleigh–Taylor instability, which arises when a denser liquid is placed on top of a lighter one, may be suppressed by vertical oscillations.² Oscillations applied parallel to the flow have also been found to suppress instabilities, for example in a viscous film flowing down an inclined plane.³ Similarly, Coward and Papageorgiou⁴ showed that the inclusion of background modulations parallel to a basic two-layer Couette flow could stabilize long wavelength instabilities driven by viscosity stratification, over a wide range of viscosity contrasts.

When superposed layers of immiscible fluids are oscillated horizontally, they are accelerated differentially because of their different densities. This results in a parallel, time-periodic shear flow, which also depends significantly on the viscosity contrast between the fluids.⁵ Interfacial instabilities in the form of standing waves have been observed in both cylindrical geometries^{6,7} and rectangular vessels,^{5,8–10} where they are commonly referred to as frozen waves. In the rectangular vessel, the presence of end walls imposes a zero horizontal volume-flux, resulting in a streamwise pressure gradient which yields counterflowing fluid layers. Lyubimov and Cherepanov¹¹ examined the stability of superposed layers of inviscid fluids contained between horizontal oscillating plates with a zero horizontal volume-flux. By decoupling fast oscillatory motion from the mean flow in the limit of large

frequencies and vanishing amplitudes of forcing, they derived, on average, a steady streamwise pressure gradient contribution to the mean flow equations. Their linear stability analysis yielded a dispersion relation analogous to the steady, inviscid Kelvin–Helmholtz instability.¹² For layer depths larger than the capillary length, the most unstable mode exhibits a finite wavelength determined by the capillary length. Khenner *et al.*¹³ extended this inviscid analysis to arbitrary frequencies and amplitudes of forcing. Similarly to Kelly¹⁴ who considered layers of infinite depth, they reduced the inviscid linear stability problem to a Mathieu equation. Thus, they found parametric resonant regions of instability associated with the intensification of the capillary-gravity waves at the interface.

In this paper, we extend the above linear stability model to include the effect of the viscosities of the liquids in layers of finite depth. Our aim is to gain an overview of the modes of instability arising in this system, and their sensitivity to the viscosity contrast. As demonstrated by the excellent quantitative agreement between experiments and computations for the onset of the short wavelength frozen wave,⁵ this viscous model is sufficient to quantitatively predict the onset of instability observed in a vessel with end walls (except in the close vicinity of the walls). In this limit, however, the neutral curves exhibit only one mode of instability in contrast with the multiple resonant parametric modes presented by Khenner *et al.*¹³ for a wide range of parameters.

In contrast with the Faraday instability,¹ the existence of a basic shear flow necessitates the numerical solution of the linearized perturbation equations governing layers of finite depth for perturbations of arbitrary wavenumber. Analytical solutions have only been obtained in the specific limits of layers of infinite depth⁷ and long wavelength perturbations.¹⁵

^{a)}Electronic mail: anne.juel@manchester.ac.uk

Kamachi and Honji¹⁵ investigated the stability to long wavelength perturbations of two fluid layers subject to a time-periodic horizontal pressure gradient in the limit of zero interfacial tension. The configuration they considered differs from our system in that the external oscillatory forcing was imposed through the pressure gradient, so that their basic flow was neither driven by the density contrast between the layers, nor required to satisfy a zero horizontal volume-flux condition. As a result, they found that layers of equal densities could become unstable provided they had different kinematic viscosities.

A numerical solution of the linear stability problem under consideration in this paper was previously obtained for arbitrary wavenumbers by Khenner *et al.*,¹³ using finite differences to approximate the spatial dependence of the flow and a Fourier expansion to resolve its time-dependence. They focused on layers of equal viscosities, but could not resolve low viscosity flows with nondimensional frequencies $\Omega = \omega d_2^2 / \nu_2 > 360$, where ω is the angular frequency of forcing, d_2 is the depth of the upper layer, and ν_2 is the kinematic viscosity of the upper layer. We employ a pseudospectral discretization scheme to approximate the spatial dependence of the perturbed flow field. Rather than integrating the resulting differential equation in time,³ we apply the fast iterative scheme introduced by Or¹⁶ to calculate the marginal stability thresholds. This method yields excellent resolution, and thus, enables us to reach the low viscosity limit with values of $\Omega < 4 \times 10^4$, as well as to investigate a wide range of viscosity contrasts ($1 \leq N_1 = \nu_2 / \nu_1 \leq 3 \times 10^4$, where ν_1 is the kinematic viscosity of the lower layer).

The model is formulated in Sec. II and details of the numerical method are presented in Sec. III. When capillary forces are significant compared to vibrational forces and the density and viscosity contrasts are moderate, our model predicts a parametric instability with neutral curves comprising successive resonant tongues. These are discussed by comparison with the linear stability predictions of the inviscid model¹³ in Sec. IV A. The lowest order mode, commonly referred to as the Kelvin–Helmholtz (KH) mode, undergoes a transition from long to finite wavelength, which is addressed in Sec. IV B, for arbitrary values of the viscosity contrast. We show in Sec. IV C that the viscous model is essential to predict the critical amplitude and most unstable wavenumber of each resonant mode accurately, particularly when the viscosity contrast is large. We find that the shape of the neutral curves varies significantly with the relative influence of capillary, gravity and vibrational forces. The thresholds of the KH mode and the first resonant mode are often of the same order, compared with the larger thresholds of the higher order resonant instabilities. Thus, we focus on the evolution of these two modes with changes in the fluid parameters in Sec. IV D. In Sec. IV D 1, the decrease in capillary forces toward the realistic values of the interfacial tension for which the frozen wave is observed, indicates the persistence of the first resonant mode and the disappearance of the KH mode usually associated with the frozen wave. The variation of the density contrast in Sec. IV D 2 yields regions where either mode is the most unstable and thus a value of $R_1 = \rho_2 / \rho_1$ (where ρ_1 and ρ_2 are the densities of the lower and upper

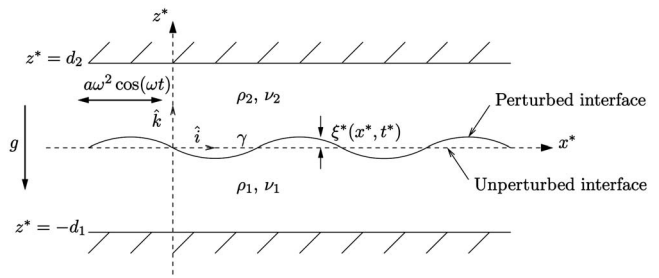


FIG. 1. Schematic diagram of the two-layer fluid system in the frame of reference of the oscillating rigid boundaries. The unperturbed interface (dashed line) coincides with the x^* axis and the perturbed interface is shown with a solid line. The superscript $*$ denotes dimensional variables.

layer, respectively) for which the threshold of both instabilities are the same. Thus, the dynamics may be affected by nonlinear interactions between these linearly unstable modes.^{17,18} Intriguingly, the two modes exhibit opposite dependencies on the viscosity contrast. Only the KH mode, which becomes increasingly unstable, persists for large values of N_1 . The respective instability mechanisms are elucidated with the time-averaged perturbation stream functions in Sec. IV D 3.

II. FORMULATION

A. Governing equations

A schematic diagram of the model is shown in Fig. 1. We consider two superposed layers of incompressible and immiscible fluids bounded above and below by rigid plates. We choose a Cartesian coordinate system where x^* is parallel to the undeformed fluid interface, which lies at $z^* = 0$, and z^* is parallel to the acceleration of gravity. The plates are oscillating sinusoidally, which in the frame of reference of the moving plates, corresponds to a sinusoidal external acceleration of the fluids in the x^* direction. The superscript $*$ denotes dimensional variables. The denser fluid is placed in the lower layer, so that the configuration is gravitationally stable. Each fluid layer is characterized by a density ρ_β , a kinematic viscosity, ν_β and a height, d_β , where the subscripts $\beta = 1, 2$ denotes the lower and upper layers, respectively. The interfacial tension between the fluids is denoted by γ . Using d_2 , $a\omega$, ω^{-1} , and $\mu_2 a \omega / d_2$, where $\mu_2 = \rho_2 \nu_2$ is the dynamic viscosity of the upper layer, as length, velocity, time, and pressure scales, respectively, the dimensionless equations governing the two-layer flow, in the frame of reference of the oscillating boundaries, are

$$\Omega \frac{\partial \mathbf{v}_\beta}{\partial t} + A \Omega (\mathbf{v}_\beta \cdot \nabla) \mathbf{v}_\beta = -R_\beta \nabla p_\beta + \frac{1}{N_\beta} \nabla^2 \mathbf{v}_\beta - \frac{G_0 \Omega}{A} \hat{\mathbf{k}} + \Omega \cos(t) \hat{\mathbf{i}}, \quad (1)$$

$$\nabla \cdot \mathbf{v}_\beta = 0, \quad (2)$$

where $\mathbf{v}_\beta = (u_\beta, w_\beta)$ is the velocity in each layer. $\Omega = (\omega d_2^2) / \nu_2$ and $A = a / d_2$ are the dimensionless frequency and amplitude of oscillation, respectively, $R_\beta = \rho_2 / \rho_\beta$ and $N_\beta = \nu_2 / \nu_\beta$, where $R_2 = N_2 = 1$, are the ratios of densities and

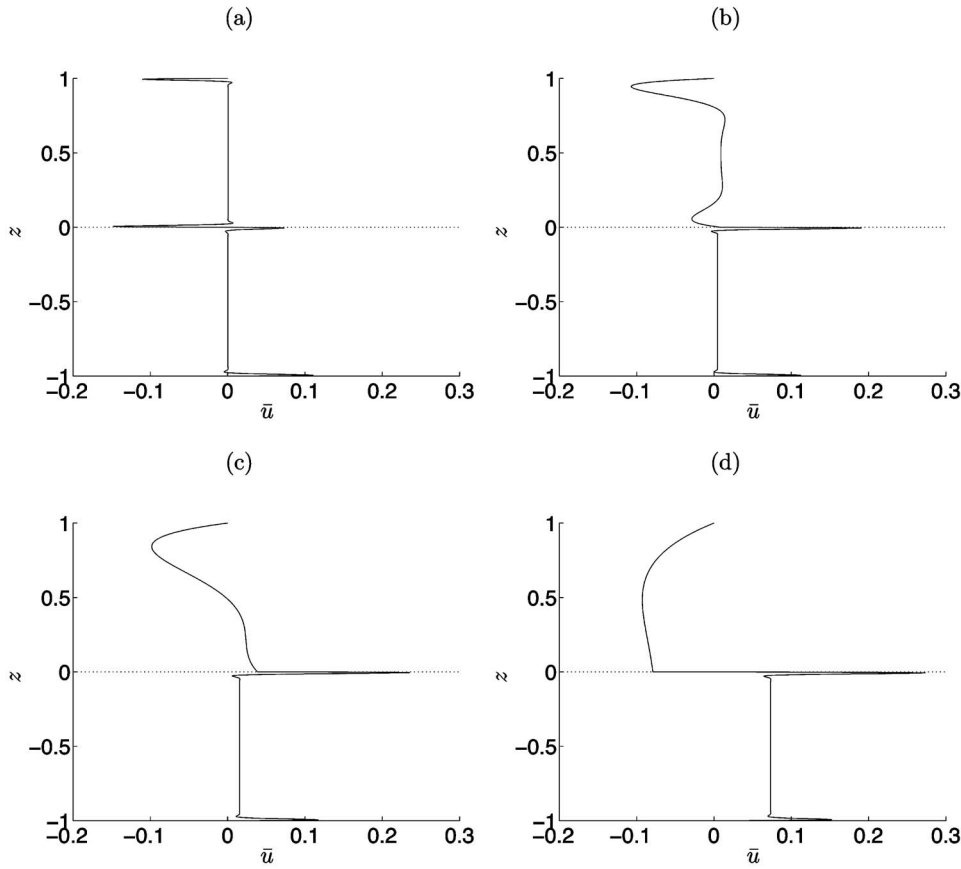


FIG. 2. Base flow solution at $t=0$, calculated for $R_1=0.49$, $G_0=1.99 \times 10^{-1}$, $\widehat{We}=2.0 \times 10^2$, $d=1$, and $A=0.4$ and different upper layer viscosities so that ΩN_1 remains constant: (a) $N_1=1$ and $\Omega=3.927 \times 10^4$; (b) $N_1=10^2$ and $\Omega=3.927 \times 10^2$; (c) $N_1=10^3$ and $\Omega=3.927 \times 10^1$; (d) $N_1=10^4$ and $\Omega=3.927$. Note the thinness of the boundary layers in the lower layer, where the nondimensional frequency is $\Omega_1=\Omega N_1=3.927 \times 10^4$.

viscosities, respectively, and $G_0=g/(d_2\omega^2)=A^2 Fr^{-1}$, where $Fr=(a\omega)^2/gd_2$, is a modified inverse Froude number.

Since the rigid boundaries are stationary in the oscillatory frame of reference, the no-slip conditions are given by

$$\mathbf{v}_1 = 0 \text{ at } z = -d \quad \text{and} \quad \mathbf{v}_2 = 0 \text{ at } z = 1, \quad (3)$$

where $d=d_1/d_2$ is the ratio of layer depths. The primitive form of the interfacial conditions, comprising the kinematic condition, the continuity of velocity, and the balance of normal and tangential stresses, at $z=\xi(x,t)$, where ξ measures the interfacial deformation, are expressed respectively as,

$$\frac{1}{A} \frac{\partial \xi}{\partial t} + (\mathbf{v}_1 \cdot \nabla) \xi = \mathbf{v}_1 \cdot \hat{\mathbf{k}}, \quad (4)$$

$$\mathbf{v}_1 = \mathbf{v}_2, \quad (5)$$

$$(\hat{\mathbf{n}} \cdot \boldsymbol{\pi}_1) \cdot \hat{\mathbf{n}} - (\hat{\mathbf{n}} \cdot \boldsymbol{\pi}_2) \cdot \hat{\mathbf{n}} = \frac{\Omega}{\widehat{We}A} \nabla \cdot \hat{\mathbf{n}}, \quad (6)$$

$$(\hat{\mathbf{t}} \cdot \boldsymbol{\pi}_1) \cdot \hat{\mathbf{n}} = (\hat{\mathbf{t}} \cdot \boldsymbol{\pi}_2) \cdot \hat{\mathbf{n}}, \quad (7)$$

$\widehat{We}=(\rho_2 d_2^3 \omega^2)/\gamma=We/A^2$, with $We=\rho_2(a\omega)^2 d_2/\gamma$, is a modified Weber number, $\boldsymbol{\pi}_\beta$ denotes the stress tensor in each fluid expressed as

$$\boldsymbol{\pi}_\beta = -p_\beta \mathbf{I} + \frac{1}{R_\beta N_\beta} [\nabla \mathbf{v}_\beta + (\nabla \mathbf{v}_\beta)^T],$$

where \mathbf{I} is the identity matrix. $\hat{\mathbf{n}}$ is the outward, normal unit vector pointing from fluid 1 into fluid 2 and $\hat{\mathbf{t}}$ is the tangent unit vector on the interface given by $\hat{\mathbf{n}}=\{-\partial\xi/\partial x, 1\}(1+(\partial\xi/\partial x)^2)^{-1/2}$ and $\hat{\mathbf{t}}=\{1, \partial\xi/\partial x\}(1+(\partial\xi/\partial x)^2)^{-1/2}$, respectively.

In addition, following Refs. 11 and 13, we enforce a zero net volume-flux in the x -direction,

$$\int_{-d}^{\xi} \mathbf{v}_1 \cdot \hat{\mathbf{i}} dz + \int_{\xi}^1 \mathbf{v}_2 \cdot \hat{\mathbf{i}} dz = 0, \quad (8)$$

in order to model the counterflowing layers generated in vessels with endwalls.

B. Base flow solution

The base flow, $(\bar{\mathbf{v}}_\beta, \bar{p}_\beta)$, is periodic, parallel to the horizontal boundaries and the interface remains unperturbed. It takes the form,

$$\bar{u}_\beta(z, t) = \Re \left[e^{it} \left(A_\beta e^{m\beta z} + i \left(\frac{SR_\beta}{\Omega} - 1 \right) + B_\beta e^{-m\beta z} \right) \right], \quad (9)$$

$$\bar{p}_\beta(z, x, t) = \Re \left[-\frac{G_0 \Omega}{R_\beta A} z + S x e^{it} + C \right], \quad (10)$$

where $m_\beta = \sqrt{i\Omega N_\beta}$ with $i = (-1)^{1/2}$, the integration constants A_β , B_β , and S are determined by imposing conditions (3), (5), (7), and (8) and C is an arbitrary constant. Their analytical form is detailed in the Appendix. Examples of base flows at $t=0$ are shown in Fig. 2 for four values of the viscosity ratio $N_1=1, 100, 1000, \text{ and } 10000$. The profiles evolve considerably in both layers despite the constant nondimensional frequency in the lower layer, $\Omega_1 = \Omega N_1 = 3.927 \times 10^4$.

C. Perturbation equations

According to Squire's theorem, which was extended to two layers by Hesla *et al.*,¹⁹ it is sufficient to consider only two-dimensional disturbances to the base flow. This choice is also justified by the experimental observation of a two-dimensional frozen wave. In deriving the stability equations, we express the governing Eqs. (1) and (2) in terms of the stream function, ψ_β , defined as

$$u_\beta = \frac{\partial \psi_\beta}{\partial z}, \quad w_\beta = -\frac{\partial \psi_\beta}{\partial x},$$

and seek a normal-mode solution²⁰ of the infinitesimally perturbed base flow of the form

$$(\psi_\beta, p_\beta, \xi) = (\bar{\psi}_\beta, \bar{p}_\beta, 0) + [\phi_\beta(z, t), P_\beta(z, t), h(t)] e^{ikx} + \text{c.c.}, \quad (11)$$

where $k = 2\pi d_2 / \lambda^*$ is the dimensionless wavenumber of the disturbance, λ^* is the dimensional wavelength, and c.c. denotes the complex conjugate. By substituting (11) into the Navier-Stokes equations (1), as well as the boundary and interfacial conditions (3)–(8), subtracting out the base state, eliminating the pressure term, and neglecting higher order terms, we obtain the following Orr-Sommerfeld equations for the two-layer flow:

$$\left(\Omega \frac{\partial}{\partial t} + ikA\Omega \bar{u}_\beta \right) (\phi_\beta'' - k^2 \phi_\beta) - ikA\Omega \bar{u}_\beta'' \phi_\beta + \frac{1}{N_\beta} (2k^2 \phi_\beta'' - k^4 \phi_\beta - \phi_\beta'''') = 0, \quad (12)$$

where the prime ($'$) denotes partial differentiation with respect to z . The no-slip boundary conditions become

$$\phi_1 = 0, \quad \phi_1' = 0 \text{ at } z = -d \quad \text{and} \quad \phi_2 = 0, \quad \phi_2' = 0 \text{ at } z = 1. \quad (13)$$

The interfacial conditions are posed at $z = \xi(x, t)$, the unknown position of the disturbed interface. However, since we are interested in the linear stability of the undisturbed interface, we can expand the flow variables and their z -derivatives as a Taylor series in ξ about $z=0$, and retain only the leading order terms in ξ . This approximation is valid provided the Taylor series remains well ordered. The linearized interfacial conditions, applied at $z=0$, become

$$\frac{1}{A} \frac{\partial h}{\partial t} + ik\bar{u}_1 h + ik\phi_1 = 0, \quad \text{kinematic condition}, \quad (14)$$

$$\phi_1' - \phi_2' + h(\bar{u}_1' - \bar{u}_2') = 0, \quad \text{continuity of velocity}, \quad (15)$$

$$\phi_1 - \phi_2 = 0, \quad \text{continuity of velocity}, \quad (16)$$

$$\left[\frac{\Omega}{R_1} \frac{\partial \phi_1'}{\partial t} - \frac{ikA\Omega}{R_1} \bar{u}_1' \phi_1 + \frac{ikA\Omega}{R_1} \bar{u}_1 \phi_1' + \frac{3k^2}{N_1 R_1} \phi_1' - \frac{1}{N_1 R_1} \phi_1''' + \frac{ikG_0 \Omega}{AR_1} h \right] - \left[\Omega \frac{\partial \phi_2'}{\partial t} - ikA\Omega \bar{u}_2' \phi_2 + ikA\Omega \bar{u}_2 \phi_2' + 3k^2 \phi_2' - \phi_2''' + \frac{ikG_0 \Omega}{A} h \right] + \frac{ik^3 \Omega}{\widehat{\text{We}} A} h = 0, \quad \text{normal stress balance}, \quad (17)$$

$$\phi_1'' + h\bar{u}_1'' + k^2 \phi_1 - N_1 R_1 (\phi_2'' + h\bar{u}_2'' + k^2 \phi_2) = 0, \quad \text{tangential stress balance}. \quad (18)$$

III. NUMERICAL SOLUTION

The partial differential system (12), with the associated boundary and interfacial conditions (13)–(18), is solved numerically for arbitrary wavenumbers using a spectral collocation scheme, and an iterative method based on Floquet theory¹⁶ to resolve the time-dependence.

A. Spatial discretization

The solution of (12) is approximated by expanding $\phi_\beta(z, t)$ as a Lagrange polynomial series, truncated at the L_β th term,

$$\phi_\beta(z, t) \approx \tilde{\phi}_\beta(z, t) = \sum_{j=0}^{L_\beta} \phi_{\beta j}(t) C_j(z), \quad (19)$$

where $\phi_{\beta j}(t)$ are the unknown time-dependent amplitudes to be determined, and $C_j(z)$ are the Lagrange basis functions defined by

$$C_j(z) = \prod_{i=0, i \neq j}^{L_\beta} \frac{z - z_i}{z_j - z_i}, \quad j = 0, 1, \dots, L_\beta, \quad (20)$$

satisfying

$$C_j(z_i) = \delta_{ij}. \quad (21)$$

In the spectral collocation method, the function $\tilde{\phi}_\beta(z, t)$ is required to satisfy Eq. (12) exactly at $L_\beta + 1$ collocation points z_i . The collocation points are chosen to be the Chebyshev-Gauss-Lobatto points defined on $[-1, 1]$, in order to achieve high resolution near the boundaries and the interface. For this purpose, the lower and upper layers are mapped onto Chebyshev space, $\zeta \in [-1, 1]$, with the transformations

$$\zeta = \frac{2z + d}{d} \quad \text{and} \quad \zeta = 1 - 2z, \quad (22)$$

respectively, so that the interface is placed at $\zeta = 1$. It follows that the system of Eqs. (12)–(18) in ζ remains the same except the n th derivative in z must be replaced by

$$\frac{\partial^n}{\partial z^n} = q_\beta^n \frac{\partial^n}{\partial \zeta^n},$$

where $q_1=2/d$ for fluid 1 and $q_2=-2$ for fluid 2. Thus, (19) becomes

$$\phi_\beta(\zeta_i, t) = \sum_{j=0}^{L_\beta} \phi_{\beta j}(t) C_j(\zeta_i), \quad i = 0, 1, \dots, L_\beta, \quad (23)$$

where

$$\zeta_i = \cos\left(\frac{\pi i}{L_\beta}\right)$$

are the Chebyshev-Gauss-Lobatto collocation points, which are the extrema of the L_β th order Chebyshev polynomial given by

$$T_{L_\beta}(\zeta) = \cos(L_\beta \cos^{-1} \zeta).$$

The Lagrange basis polynomials based on the Chebyshev-Gauss-Lobatto collocation points are defined by

$$C_j(\zeta) = \frac{(-1)^j(\zeta^2 - 1)T'_{L_\beta}(\zeta)}{\bar{c}_j L_\beta^2(\zeta - \zeta_j)}, \quad j = 0, 1, \dots, L_\beta,$$

where $\bar{c}_0 = \bar{c}_{L_\beta} = 2$ and $\bar{c}_1 = \dots = \bar{c}_{L_\beta-1} = 1$.

Differentiation of ϕ_β with respect to ζ is expressed in terms of the derivatives of the basis functions evaluated at the collocation points,

$$\frac{\partial^n}{\partial \zeta^n} \phi_\beta(\zeta_i, t) = \sum_{j=0}^{L_\beta} \phi_{\beta j}(t) D_{ij}^n, \quad (24)$$

where

$$D_{ij}^n = q_\beta^n \frac{\partial^n}{\partial \zeta^n} (C_j(\zeta_i)), \quad n \geq 1, \quad i, j = 0, 1, \dots, L_\beta.$$

i, j are the row and column indices of the n th order derivative matrix D_{ij}^n , respectively. The first order derivative matrix, D_{ij} , for the Chebyshev-Gauss-Lobatto collocation points can be written in explicit form as

$$D_{ij} = \begin{cases} \frac{\bar{c}_i(-1)^{i+j}}{\bar{c}_j(\zeta_i - \zeta_j)} & \text{if } i \neq j, \\ -\frac{2L_\beta^2 + 1}{6} & \text{if } i = j = L_\beta, \\ \frac{2L_\beta^2 + 1}{6} & \text{if } i = j = 0, \\ -\frac{\zeta_j}{2(1 - \zeta_j^2)} & \text{if } 1 \leq i = j \leq L_\beta - 1. \end{cases} \quad (25)$$

Higher order derivatives are multiple powers of D_{ij} , that is,

$$q_\beta^n \frac{\partial^n}{\partial \zeta^n} (C_j(\zeta_i)) = q_\beta^n D_{ij}^n = q_\beta^n (D_{ij})^n, \quad (26)$$

where $(D_{ij})^n$ is the n th power of the matrix element D_{ij} .

Following Lanczos's method,²¹ the governing equations (12) are evaluated at $\zeta = \zeta_i$,

$$\begin{aligned} & [\Omega(q_\beta^2 D_{ij}^2 - k^2 I_{ij})] \left[\frac{\partial \phi_{\beta i}}{\partial t} \right] \\ &= \left[\frac{1}{L_\beta} q_\beta^4 D_{ij}^4 - \left(\frac{2}{L_\beta} k^2 + ikA\Omega \bar{u}_{\beta i} \right) q_\beta^2 D_{ij}^2 \right. \\ & \quad \left. + \left(\frac{1}{L_\beta} k^4 + ik^3 A\Omega \bar{u}'_{\beta i} + ikA\Omega \bar{u}''_{\beta i} \right) I_{ij} \right] [\phi_{\beta j}], \quad (27) \end{aligned}$$

where $i=2, 3, \dots, L_\beta-2, j=0, 1, \dots, L_\beta$ and I is the identity matrix, and the boundary conditions (13)–(18) are evaluated at the boundary collocation points $\zeta=1$ and $\zeta=-1$,

$$[I_{L_\beta j}] [\phi_{\beta j}] = 0, \quad (28)$$

$$[q_\beta D_{L_\beta j}] [\phi_{\beta j}] = 0, \quad (29)$$

$$\frac{1}{A} \frac{\partial h}{\partial t} = [-ikI_{0j}, -ik\bar{u}_{10}] \begin{bmatrix} \phi_{1j} \\ h \end{bmatrix}, \quad (30)$$

$$[q_1 D_{0j}, -q_2 D_{0j}, \bar{u}'_{10} - \bar{u}'_{20}] \begin{bmatrix} \phi_{1j} \\ \phi_{2j} \\ h \end{bmatrix} = 0, \quad (31)$$

$$[I_{0j}, -I_{0j}] \begin{bmatrix} \phi_{1j} \\ \phi_{2j} \end{bmatrix} = 0, \quad (32)$$

$$\begin{aligned} & \left[\frac{\Omega}{R_1} q_1 D_{0j}, -\Omega q_2 D_{0j}, 0 \right] \begin{bmatrix} \partial \phi_{1j} / \partial t \\ \partial \phi_{2j} / \partial t \\ \partial h / \partial t \end{bmatrix} \\ &= \left[\frac{1}{N_1 R_1} (q_1^3 D_{0j}^3 - 3k^2 q_1 D_{0j}) - \frac{i}{R_1} kA\Omega \bar{u}_{10} q_1 D_{0j} \right. \\ & \quad \left. + ikA\Omega \bar{u}'_{10} I_{0j} - q_2^3 D_{0j}^3 + 3k^2 q_2 D_{0j} + ikA\Omega \bar{u}_{20} q_2 D_{0j} \right. \\ & \quad \left. - ikA\Omega \bar{u}'_{20} I_{0j}, \frac{ik}{A} \left(\left(1 - \frac{1}{R_1} \right) G_0 \Omega - k^2 \frac{\Omega}{We} \right) \right] \begin{bmatrix} \phi_{1j} \\ \phi_{2j} \\ h \end{bmatrix}, \quad (33) \end{aligned}$$

$$\begin{aligned} & \left[\frac{1}{N_1 R_1} (q_1^2 D_{0j}^2 + k^2 I_{0j}), - (q_2^2 D_{0j}^2 + k^2 I_{0j}), \frac{1}{N_1 R_1} \bar{u}''_{10} - \bar{u}''_{20} \right] \\ & \quad \times \begin{bmatrix} \phi_{1j} \\ \phi_{2j} \\ h \end{bmatrix} = 0. \quad (34) \end{aligned}$$

Thus, we obtain an $(L_1 + L_2 + 3) \times (L_1 + L_2 + 3)$ system of the form

$$\mathbf{B} \frac{\partial \mathbf{x}}{\partial t} = (\mathbf{M}_0 + \mathbf{M}(t)) \mathbf{x}, \quad (35)$$

where \mathbf{x} is the unknown vector

$$\mathbf{x}(t) = (\phi_{10}, \phi_{11}, \dots, \phi_{1L_1}, \phi_{20}, \phi_{21}, \dots, \phi_{2L_2}, h)^T(t),$$

$\mathbf{M}(t) = \mathbf{M}_s \sin(t) + \mathbf{M}_c \cos(t)$ is a 2π -periodic matrix, and \mathbf{B} and \mathbf{M}_0 are constant coefficient matrices.

B. Temporal solution

The Floquet problem (35) is solved using a fast iterative scheme based upon the Newton-Raphson method that was developed by Or¹⁶ for a viscous single layer under oscillating shear. According to Floquet theory,²² the solution of (35) is of the form

$$\mathbf{x}(t) = Z(t)\exp(\sigma t), \quad (36)$$

where $Z(t)$ is a 2π -periodic vector function and σ is the Floquet exponent. $Z(t)$ is expanded as a complex Fourier series, truncated at order K , so that

$$\mathbf{x}(t) = \sum_{n=-K}^K \mathbf{x}_n e^{int+\sigma t}, \quad (37)$$

where $\sigma = \sigma_r + i\sigma_i$ and \mathbf{x}_n are constant vector coefficients, and substituted into the differential Eq. (35). We focused on harmonic solutions with $\sigma_i = 0$ because subharmonic solutions are not generally found in this system due to constraints imposed by the conjugate-translation symmetry.²³ By substituting solution (37) into Eq. (35) and employing the iterative procedure of Or,¹⁶ we obtained the following polynomial eigenvalue equation of order $K+1$ on x_0 ,

$$\{(\mathbf{M}_0 - \mathbf{B}\sigma) + (\mathbf{M}^* \mathbf{R}_{-1}(\sigma) + \mathbf{M} \mathbf{R}_1(\sigma))\} \mathbf{x}_0 = 0, \quad (38)$$

where $\mathbf{M} = \frac{1}{2}(\mathbf{M}_c + i\mathbf{M}_s)$ and \mathbf{M}^* denotes the complex conjugate of \mathbf{M} . Within the formulation of (38) we have used the following recurrence relations: for $1 \leq n \leq K-1$,

$$\mathbf{x}_n = \mathbf{R}_n \mathbf{x}_{n-1}, \quad \mathbf{R}_n = -(\mathbf{M}_0 - \mathbf{B}(in + \sigma) + \mathbf{M} \mathbf{R}_{n+1})^{-1} \mathbf{M}^*,$$

$$\begin{aligned} \mathbf{x}_{-n} = \mathbf{R}_{-n} \mathbf{x}_{-(n-1)}, \quad \mathbf{R}_{-n} = -(\mathbf{M}_0 - \mathbf{B}(-in + \sigma) \\ + \mathbf{M}^* \mathbf{R}_{-(n+1)})^{-1} \mathbf{M}, \end{aligned}$$

and for $n=K$,

$$\mathbf{x}_K = \mathbf{R}_K \mathbf{x}_{K-1}, \quad \mathbf{R}_K = -(\mathbf{M}_0 - \mathbf{B}(iK + \sigma))^{-1} \mathbf{M}^*,$$

$$\mathbf{x}_{-K} = \mathbf{R}_{-K} \mathbf{x}_{-(K-1)}, \quad \mathbf{R}_{-K} = -(\mathbf{M}_0 - \mathbf{B}(-iK + \sigma))^{-1} \mathbf{M}^*.$$

Equation (38) admits a nontrivial solution if and only if the determinant vanishes.

To locate the critical values of A , A_c , on the marginal stability curve, we fixed $(\Omega, R_1, N_1, \widehat{We}, G_0, d, k, \sigma_i = 0)$ and incremented the value of A from $A_0 = 0.001$ until we identified the value of A for which the growth rate, σ_r , satisfying Eq. (38), first crossed zero. σ_r was obtained by iteration of a suitable initial guess, $\sigma_{\text{guess}} = 2$. This value was found to be suitable for the entire parameter range investigated, since the system was only solved up to the point of marginal stability, i.e., for values of A , $A_0 \leq A \leq A_c$. By iterating on σ_{guess} , we evaluated successive values of the determinant and determined an estimate of σ_r accurate to two decimal places, σ_{approx} , at which the determinant first crossed zero. The application of a Newton-Raphson iteration to σ_{approx} yielded σ_r for each value of A . Once the first zero-crossing of σ_r was located, the associated eigenvector x_0 was evaluated using singular value decomposition (x_0 is the singular vector corresponding to the smallest singular value).

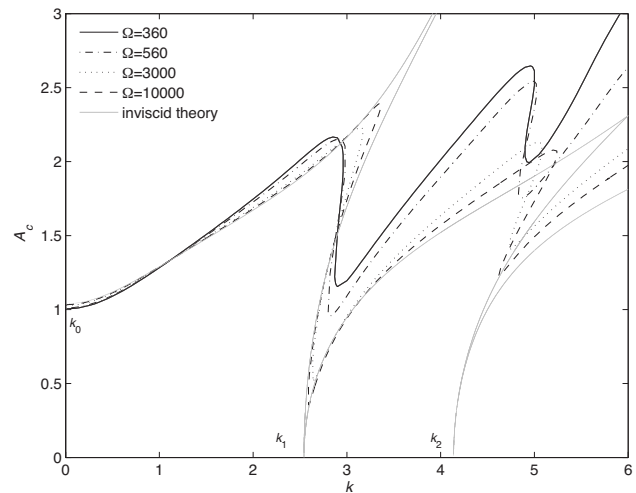


FIG. 3. Marginal stability curves showing the critical amplitude, A_c , against the wavenumber, k for $3.6 \times 10^2 \leq \Omega \leq 10^4$. The other parameter values are $R_1 = 5 \times 10^{-1}$, $N_1 = 1$, $G_0 = 1.60 \times 10^{-1}$, $\widehat{We} = 6.25$ and $d = 1$. The inviscid prediction of Ref. 13 is plotted for comparison with a gray line. Note that these flow parameters are the same as in Ref. 13 (Fig. 7).

In order to reconstruct the stream function in each layer, ϕ_β , the solution vector, $\mathbf{x}(t)$, was formed using Eq. (37) and the relevant component part substituted into Eq. (23). The remaining Fourier vector components, $-K < \mathbf{x}_n < K$, were determined using the recurrence relations give above.

C. Convergence tests and validation of the code

All numerical computations were carried out in MATLAB. Each linear stability result was checked for convergence by consecutively increasing the number of Fourier modes and the number of Chebyshev modes in the lower and upper layers by 2. The calculations were subsequently performed with the minimum number of Fourier and Chebyshev modes required to reach linear stability results accurate to the third decimal point. The number of Chebyshev polynomials required for a converged solution increased with the nondimensional frequencies in each layer, $\Omega_2 = \Omega$ and $\Omega_1 = \Omega N_1$, because the boundary layer thicknesses are reduced. The spacing of the Gauss-Lobatto-Chebyshev collocation points near the boundaries is $\mathcal{O}(M_\beta^{-2})$, and it was found that at least one collocation point had to lie within the boundary layer to ensure the convergence of the solution. The results presented in this paper were calculated for $74 < N_1 < 148$, $30 < N_2 < 90$, and $K = 14$. The code was validated by successfully reproducing several known results for both oscillatory single-layer and two-layer flows. The stability results obtained using the Chebyshev collocation code were found to be in excellent agreement with those of Ref. 13 in the limit of large viscosities ($\Omega < 250$). We were also able to reproduce Or's¹⁶ results by setting the upper layer flow parameters to that of air ($\nu_2 = 15.11 \times 10^{-6} \text{ m}^2 \text{ s}^{-1}$ and $\rho_2 = 1.29 \text{ kg m}^{-3}$), and omitting condition (8).

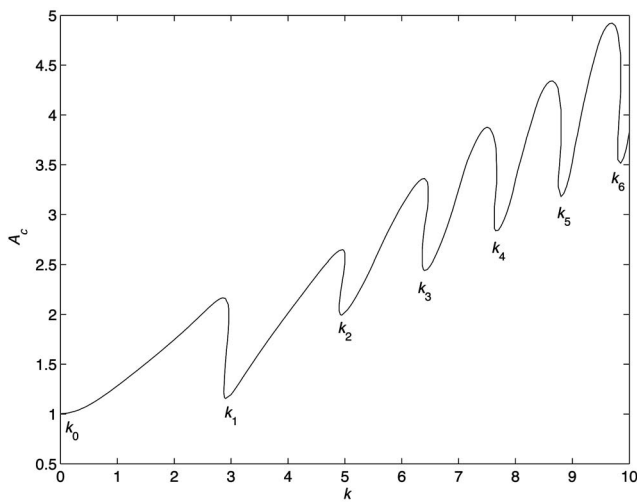


FIG. 4. Neutral curve showing the first seven instability tongues (k_0, k_1, \dots, k_6) for $\Omega=3.6 \times 10^2$, $R_1=5 \times 10^{-1}$, $N_1=1$, $G_0=1.60 \times 10^{-1}$, $We=6.25$, and $d=1$.

IV. RESULTS

A. Parametric instability

We determined the critical value of the amplitude of oscillation, A_c , at which the parallel shear flow becomes unstable to standing waves of wavenumber k . A series of neutral stability curves is shown in Fig. 3 for fluids of equal but decreasing viscosities, i.e., $N_1=1$ and increasing Ω . Whereas Khenner *et al.*¹³ were unable to resolve calculations for $\Omega > 3.6 \times 10^2$, the pseudospectral method employed here allows us to reach values of up to $\Omega=4 \times 10^4$, which is the largest value presented in this paper. Each curve separates the (A_c, k) -plane into a region of stable solutions (below the curve) and unstable (growing) harmonic solutions (above the

curve). As Ω increases, the marginal stability curves converge toward the stability boundaries of the inviscid model,¹³ which are shown with gray lines in Fig. 3. The inviscid stability boundaries were obtained by Floquet analysis of the Mathieu equation¹³ and comprise a succession of tongues of harmonic response, i.e., of the same period as that of the external oscillatory drive. The long wavelength mode ($k_0=0.001$, which was the minimum value of k used in the calculations) in Fig. 3 is primarily due to the average effect of the oscillatory drive and is associated with a Kelvin–Helmholtz instability mechanism.¹³ The tongues (centered on the modes k_1 and k_2) delimit the first two regions of resonant response of the flow. As A_c tends to zero, the resonant response approaches a single Fourier mode, while at finite A_c results from the superposition of several Fourier modes; see Fig. 5(a). The convergence of the viscous stability results toward the inviscid result as Ω increases suggests a similar parametric instability in the viscous model. Although the long-wavelength KH instability is virtually independent of viscosity, the resonant response at finite wavelength, centered on the modes k_1 and k_2 , is strongly stabilized by increasing the viscosity of both layers, and the most unstable wavenumbers k_1 and k_2 are displaced toward higher values of k . This dependence on viscosity is similar to that uncovered by Kumar and Tuckerman¹ in their stability analysis of the Faraday problem with equal viscosity layers.

In Fig. 4, the neutral curve plotted in Fig. 3 for $\Omega=360$ is extended to wavenumbers up to $k=10$. It exhibits a succession of local minima at k_0, k_1, \dots, k_6 , including a long-wavelength KH instability and six resonant tongues. The time dependence of the solution at the first four minima is shown in Fig. 5(a). In the presence of viscosity, A_c is finite at each local minimum, and the temporal dependence of the neutral solution is a superposition of several Fourier modes. The temporal response for the instability modes k_0 and k_1 is

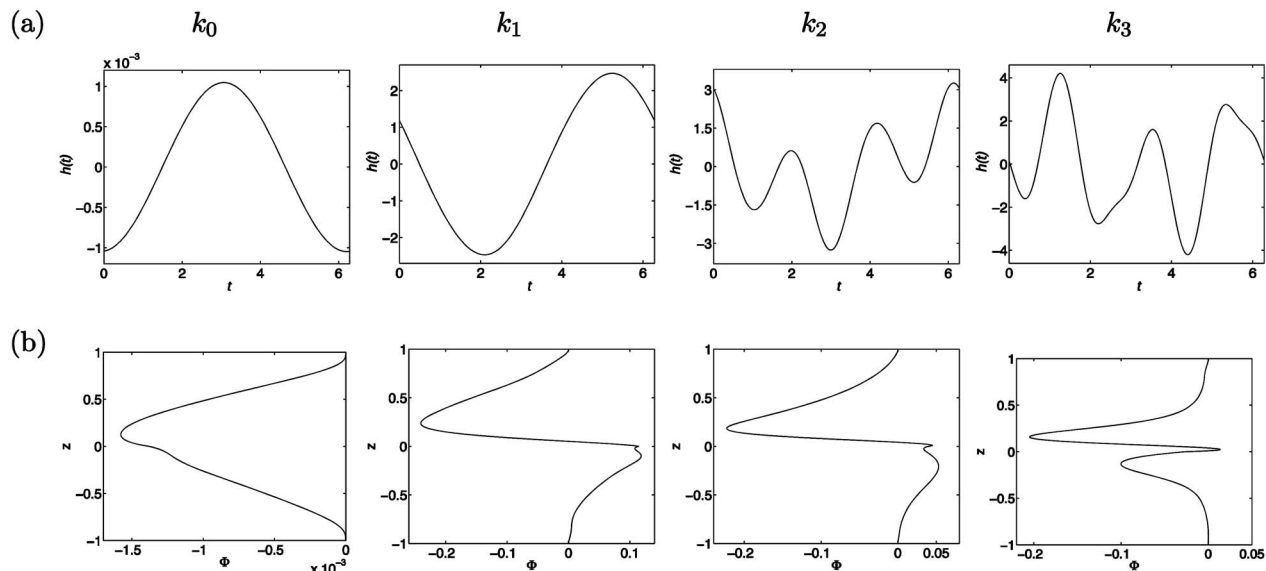


FIG. 5. (a) Interface height versus time: time-series of the eigenfunction at the modes k_0-k_3 in Fig. 4. (b) Time-averaged perturbation stream functions at the modes k_0-k_3 in Fig. 4.

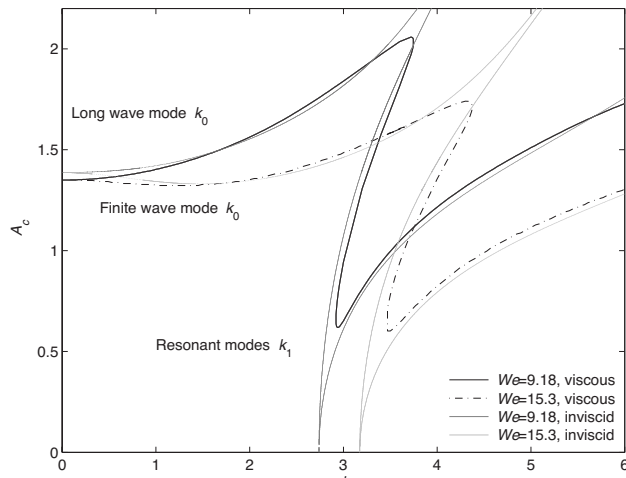


FIG. 6. Neutral curves for $\widehat{We}=9.18$ and 15.3 . The other parameter values are $R_1=4.90 \times 10^{-1}$, $N_1=10^2$, $\Omega=2.11 \times 10^2$, $G_0=2.91 \times 10^{-1}$, and $d=1$. The corresponding inviscid results (Ref. 13) are plotted for comparison with gray lines.

approximately sinusoidal, whereas Fourier modes of up to order three and five contribute significantly to the time-dependence of the response of the instability modes k_2 and k_3 , respectively. The form of the time-averaged perturbation stream function, whose physically significant real part is plotted in Fig. 5(b), changes continuously with k . The stream function at k_0 exhibits on average a single peak across the two layers, centered near the interface, which indicates on average a single vortex acting to deform the interface. The peaks in the perturbation stream functions of the modes k_1 and k_2 indicate the presence of counter-rotating vortices on either side of the interface, so that the interfacial deformation is driven on average by the net difference in vorticity on both sides (see Sec. IV D 3 for further details on the interpretation of the stream function plots). The instability corresponding to k_3 has a more complex structure, whereby co-rotating vortices in each layer are separated by a thin, counter-rotating vortex near the interface in the upper layer. Although the perturbation is distributed across the entire channel in the case of the long-wavelength mode (k_0), the peaks are increasingly concentrated near the interface for higher values of k , so that the instability is clearly interfacial, similarly to the “soft” wave uncovered by Kamachi and Honji.¹⁵

In Fig. 4, the mode k_0 corresponds to the absolute minimum of the neutral stability curve and thus, a long-wavelength instability is excited at onset. While the thresholds of the modes k_n ($n \geq 2$) are always higher than that of k_1 , either k_0 or k_1 may be the most unstable modes depending on the values of parameters. We examine this competition in further detail in Sec. IV D.

B. Long versus finite wave instability

Depending on the choice of parameters, the mode k_0 may be found at $k=0.001$ (the minimum value of k for which calculations were performed, i.e. long wavelength) or at $k > 0.001$ (finite wavelength). An example is given in Fig. 6 where $k_0=0.001$ for $\widehat{We}=9.18$, but $k_0 > 0.001$ for $\widehat{We}=15.3$.

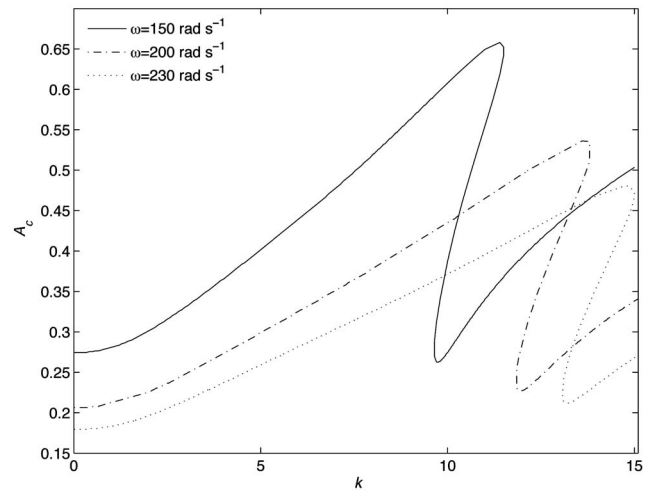


FIG. 7. Neutral curves for increasing frequencies of forcing: (—) $\Omega=1.1 \times 10^3$, $G_0=1.16 \times 10^{-2}$, $\widehat{We}=2.29 \times 10^2$, (---) $\Omega=1.4 \times 10^3$, $G_0=6.5 \times 10^{-3}$, $\widehat{We}=4.08 \times 10^2$, (···) $\Omega=1.6 \times 10^3$, $G_0=4.9 \times 10^{-3}$, $\widehat{We}=5.40 \times 10^2$. The other parameter values are $N_1=100$, $R_1=4.90 \times 10^{-1}$, and $d=1$.

A selection criterion was established by Khenner *et al.*¹³ for finite-depth layers of inviscid fluids. In our notation, if $H=d_2/\sqrt{\gamma/((\rho_1-\rho_2)g)}$ is the layer height scaled by the capillary length (H is also the capillary wavenumber in our formulation), finite wavelength KH instabilities are only found if $H > \sqrt{3}$ and

$$\widehat{We} < \widehat{We}^* = \frac{64(H^2 - 3)^2(1 + R_1)^2}{9H^2(1 - R_1)^3 G_0^3}.$$

Our calculations suggest that this criterion remains valid for the viscous analysis when $N_1=1$. When $N_1 \neq 1$, however, we find that this criterion is no longer strictly valid. For example, for $\widehat{We}=10$, $R_1=4.90 \times 10^{-1}$, $N_1=10^2$, $G_0=1.99 \times 10^{-1}$, $\Omega=1.57 \times 10^2$, and $d=1.0$ (see Fig. 9 below), $H=1.43 < \sqrt{3}$ but $k_0=0.3 > 0.001$. This is not surprising since the viscosity contrast affects the most unstable wavenumber of the frozen wave significantly (see Ref. 5, Fig. 7). The effect of the viscosity contrast on the neutral curves is discussed further in Secs. IV C and IV D 3.

The long wavelength instability is virtually independent of individual changes in \widehat{We} , Ω , and N_1 , but depends strongly on the value of the modified inverse Froude number, G_0 , indicating that gravity acts to stabilize long wavelength perturbations. Thus, an increase in the frequency of forcing ω , which corresponds to increasing Ω and \widehat{We} , while decreasing G_0 , destabilizes the limit of small k more strongly than the resonant modes at higher k , whose most unstable wavenumbers also increase significantly with frequency (see Fig. 7). Thus, in the limit of large frequencies, the KH instability (mode k_0) is observed at the onset, thus validating the results of the time-averaged model of Lyubimov and Cherepanov.¹¹ A similar decrease of the threshold of the long wave instability with increasing frequency was also found by Kamachi and Honji.¹⁵

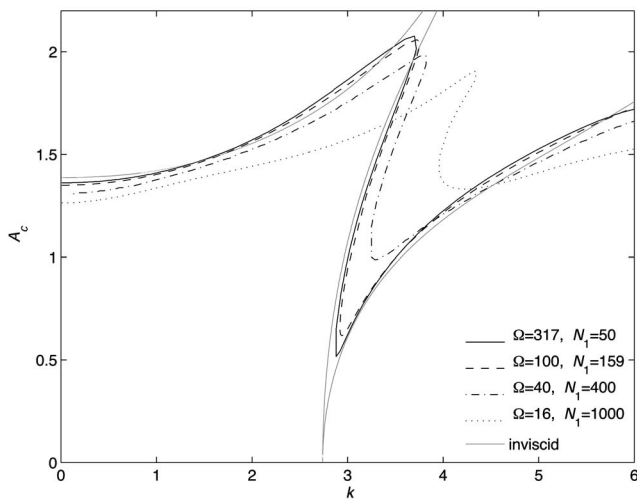


FIG. 8. Neutral curves for $\widehat{We}=9.18$ and fluid layers of unequal viscosities. The viscosity contrast is increased by increasing the viscosity of the upper layer. Thus, N_1 increases and Ω decreases. The other parameter values are $R_1=4.90 \times 10^{-1}$, $G_0=2.91 \times 10^{-1}$, and $d=1$. The inviscid result (Ref. 13) is plotted for comparison with a gray line.

C. Fluids of unequal viscosities

In experimental flows^{5,10,9} the viscosities of the fluids are generally different, and the viscosity ratio can be large. Thus, we focus hereafter on the general case where $N_1 \neq 1$. Talib *et al.*⁵ have shown that the instability threshold is surprisingly reduced over a wide range of viscosity contrasts, when N_1 is raised by increasing the viscosity of either layer. Over the range of N_1 investigated in Ref. 5, $1 \leq N_1 \leq 6 \times 10^4$, the nonmonotonic variation of the most unstable critical amplitude and wavenumber with N_1 is reflected in the average perturbation stream function. The neutral curves shown in Fig. 8 are for increasing viscosity contrasts achieved by increasing the viscosity of the upper layer similarly to Ref. 5, so that $50 \leq N_1 \leq 10^3$ and $3.17 \times 10^2 \geq \Omega \geq 16$. The value of the wavenumber k_1 increases with viscosity contrast. This effect is much stronger than when both viscosities were increased simultaneously in Fig. 3, i.e., Ω reduced with $N_1=1$. Thus, the inviscid theory is unsuitable to model parametric instabilities in viscous layers, since it can neither predict the instability threshold, nor the value of the most unstable wavenumber of the parametric modes.

It is interesting to note that we have not been able to find any set of parameters corresponding to realistic fluid properties, where the neutral curve comprises more than a single minimum. The parameters chosen for all the calculations shown above correspond to physically unrealizable fluid properties. In order to achieve the moderate values of the modified Weber number ($\widehat{We} \lesssim 750$) necessary for multiple resonances to emerge while retaining experimentally practical frequencies of forcing, the interfacial tension has to be at least one to two orders of magnitude larger than that measured in common pairs of liquids. In Sec. IV D, we investigate the changes in the neutral curves when the physical parameters R_1 , \widehat{We} , and N_1 are varied, and determine limits where the multiple minima vanish.

D. Parameter study of the finite-wave instabilities

The large number of nondimensional groups (7) governing the dynamics prohibits an exhaustive investigation of linear solution classes. In order to establish the physical significance of the k_0 and k_1 modes, it is convenient to restrict our attention to flows based on the physical properties of a perfluorinated liquid (Flutec PP9) in the lower layer ($\rho_1=1.973 \times 10^3 \text{ kg m}^{-3}$, $\nu_1=2.0 \times 10^{-6} \text{ m}^2 \text{ s}^{-1}$) and silicone oil in the upper layer ($\rho_2=9.670 \times 10^2 \text{ kg m}^{-3}$, $\nu_2=2.0 \times 10^{-4} \text{ m}^2 \text{ s}^{-1}$). The interfacial tension between the layers is taken to be $\gamma=4.0 \times 10^{-3} \text{ N m}^{-1}$, from the measurements of interfacial tensions for similar pairs of fluids.^{5,10} Layer heights of $d_1=d_2=0.05 \text{ m}$ and an angular velocity of $\omega=10\pi \text{ rad s}^{-1}$ yield the following nondimensional parameters: $R_1=4.90 \times 10^{-1}$, $\widehat{We}=2.98 \times 10^4$, $N_1=10^2$, $G_0=1.99 \times 10^{-1}$, $\Omega=3.927 \times 10^2$ and $d=1.0$. For these values of parameters, the neutral curve (A_c, k) exhibits a single minimum at a nonzero value of k . In order for local minima corresponding to the k_0 and k_1 modes to emerge, the interfacial tension needs to be significantly increased so that $\widehat{We} \lesssim 7.5 \times 10^2$ (see Sec. IV C). We choose $\gamma=5.96 \times 10^{-1} \text{ N m}^{-1}$ (which is approximately two orders of magnitude larger than the interfacial tension measured between Flutec PP9 and silicone oil), i.e., $\widehat{We}=2.0 \times 10^2$, and investigate the evolution of the k_0 and k_1 instabilities with changes in the density contrast (R_1) and viscosity contrast (N_1 and Ω).

1. Dependence on interfacial tension

For $\gamma=5.965 \times 10^{-1} \text{ N m}^{-1}$ ($\widehat{We}=200$) and $\gamma=1.988 \times 10^{-1} \text{ N m}^{-1}$ ($\widehat{We}=600$), which correspond to unphysically large values of the interfacial tension, both the modes k_0 and k_1 are found in the neutral curves shown in Fig. 9(a). An examination of the eigenmodes reveals that for $\gamma=1.193 \times 10^{-1} \text{ N m}^{-1}$ ($\widehat{We}=1000$) and $\gamma=5.965 \times 10^{-2} \text{ N m}^{-1}$ ($\widehat{We}=2000$), only the k_1 mode remains. Note that all the critical amplitudes converge to the same value as k tends to zero. This is because long wavelength perturbations of the interface are virtually independent of interfacial tension, which like viscosity, predominantly acts on the growth of short wavelength disturbances. Note also the presence of the k_2 mode for $\gamma=5.965 \times 10^{-1} \text{ N m}^{-1}$. The minimum of the neutral curve indicating this parametric-resonance mode vanishes for decreasing values of γ .

As seen in Fig. 9(c), the wavenumber of the KH mode (k_0) remains approximately constant with respect to the capillary wavenumber denoted by $H=d_2\sqrt{g(\rho_1-\rho_2)/\gamma}$, while the relative wavenumber k_1/H increases monotonically with γ . Although the dimensional critical amplitudes of the modes k_0 and k_1 , denoted by a_0 and a_1 , respectively, and shown in Fig. 9(b), both decrease as γ is reduced, a_0 decays rapidly and converges towards a_1 , until it vanishes for $\gamma \lesssim 2.0 \times 10^{-1} \text{ N m}^{-1}$. Thus, the k_1 mode is the most unstable over the entire range of γ investigated. Note that it is the k_1 mode which persists when γ is reduced toward experimental values [first point in Figs. 9(b) and 9(c)], rather than the k_0 mode generally associated with the KH instability.^{11,13}

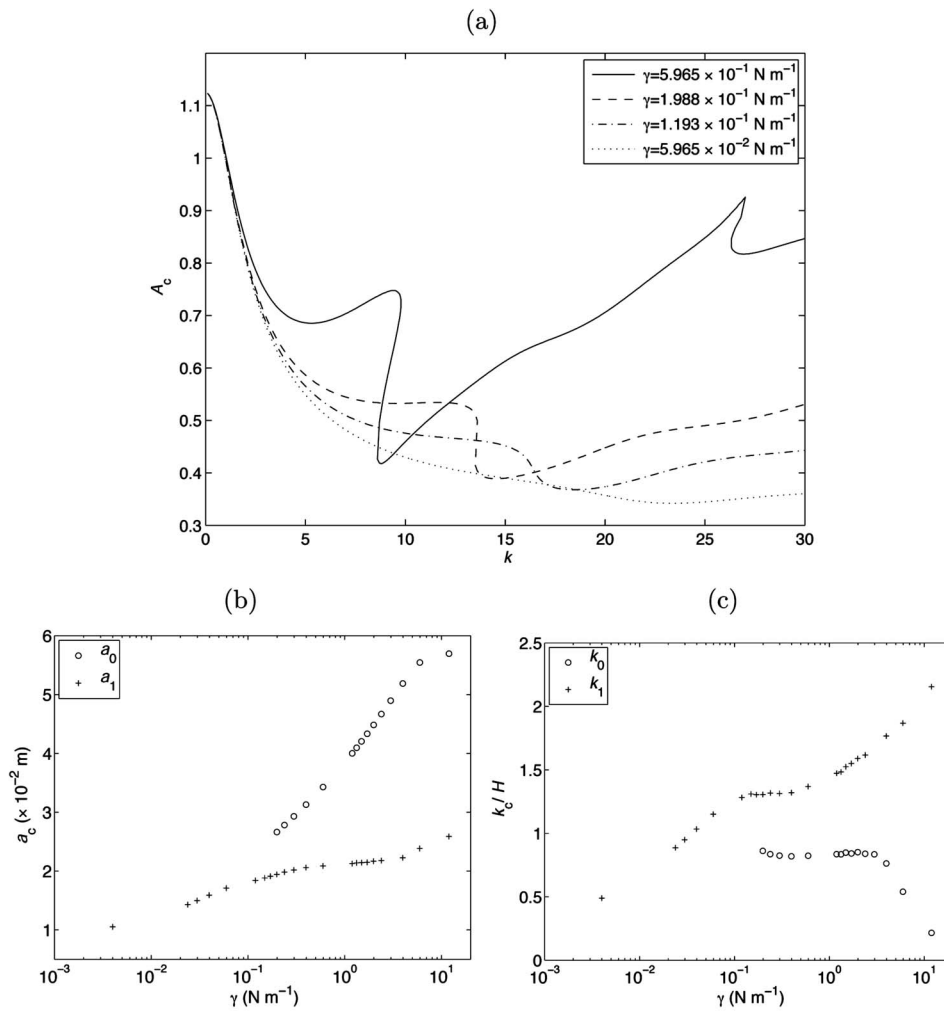


FIG. 9. (a) Neutral curves (A_c, k) for $\widehat{We} = 2 \times 10^2$, 6×10^2 , 1×10^3 , and 2×10^3 . (b) Dependence of the dimensional critical amplitudes of the modes k_0 and k_1 on interfacial tension. (c) Dependence on interfacial tension of k_0 and k_1 relative to the capillary wavenumber. The other parameter values are $R_1 = 4.90 \times 10^{-1}$, $N_1 = 10^2$, $G_0 = 1.99 \times 10^{-1}$, $\Omega = 1.57 \times 10^2$, and $d = 1.0$. The first point in both (b) and (c) corresponds to the experimental value of the interfacial tension for Flutec PP9 and silicone oil discussed in Sec. IV D, $\gamma = 4 \times 10^{-1} \text{ N m}^{-1}$ ($\widehat{We} = 2.98 \times 10^4$).

2. Density contrast

The density contrast is varied by changing the density of the lower layer, ρ_1 , which yields a change in the nondimensional parameter $R_1 = \rho_2 / \rho_1$ only. A series of four neutral curves (A_c, k) are shown in Fig. 10(a). The shape of the neutral curves evolves considerably when R_1 is decreased from 0.58 to 0.1. For $R_1 = 0.58$ and 0.4, there are two local minima corresponding to the modes of instability k_0 and k_1 , but for $R_1 = 0.2$ and 0.1 only the local minimum associated with k_1 remains. Detailed plots of the critical amplitudes and wavenumbers of the modes k_0 and k_1 are shown in Figs. 10(b) and 10(c). A_0 and A_1 both increase monotonically when the density contrast is reduced, i.e., R_1 increases. The mode k_1 is generally the onset mode except for fluids of nearly equal densities ($R_1 = 0.9$), where the mode k_0 is most unstable. The crossover of the (A_c, R_1) curves occurs between $R_1 = 0.8$ and 0.9, so nonlinear mode interaction may prevail in this region.^{17,18} Note that for $R_1 = 1$, there is no flow nor instability.

While the wavenumber of the mode k_0 remains close to the capillary wavenumber H , the wavenumber of k_1 decreases strongly to values below that of H when R_1 is decreased, resulting in the disappearance of the mode k_0 for $R_1 \leq 0.3$. Although the threshold of the mode k_1 decreases monotonically over the entire range of R_1 investigated, the

neutral curve shown in Fig. 10(a) for $R_1 = 0.1$ is located mostly above that for $R_1 = 0.2$, and thus indicates a tendency towards restabilization as R_1 decreases strongly. Although the density contrast enables the relative acceleration of the fluid layers, the stable density stratification also induces stabilizing buoyancy forces. Thus, decreasing R_1 lowers the instability threshold except for small values of R_1 , i.e., very different densities, where the flow is increasingly stabilized. A qualitatively similar dependence of the instability threshold on R_1 is predicted by Ref. 11 in the case of the time-averaged counterflow of inviscid fluids in the limit of high frequencies and vanishing amplitudes of forcing.

3. Viscosity contrast

The most intriguing behavior is found when varying the viscosity contrast. As in Sec. IV C, we choose to increase the viscosity contrast by increasing the viscosity of the upper layer beyond that of the lower layer, which is kept constant. This leads to a combined increase in N_1 and decrease in Ω . This means that the nondimensional frequency (analogous to a Reynolds number divided by A) in the upper layer, $\Omega_2 = \Omega$, decreases while the nondimensional frequency in the lower layer, $\Omega_1 = \Omega N_1$ remains constant.

In Fig. 11(a), neutral curves calculated for increasing viscosity contrasts indicate that the k_1 mode is increasingly

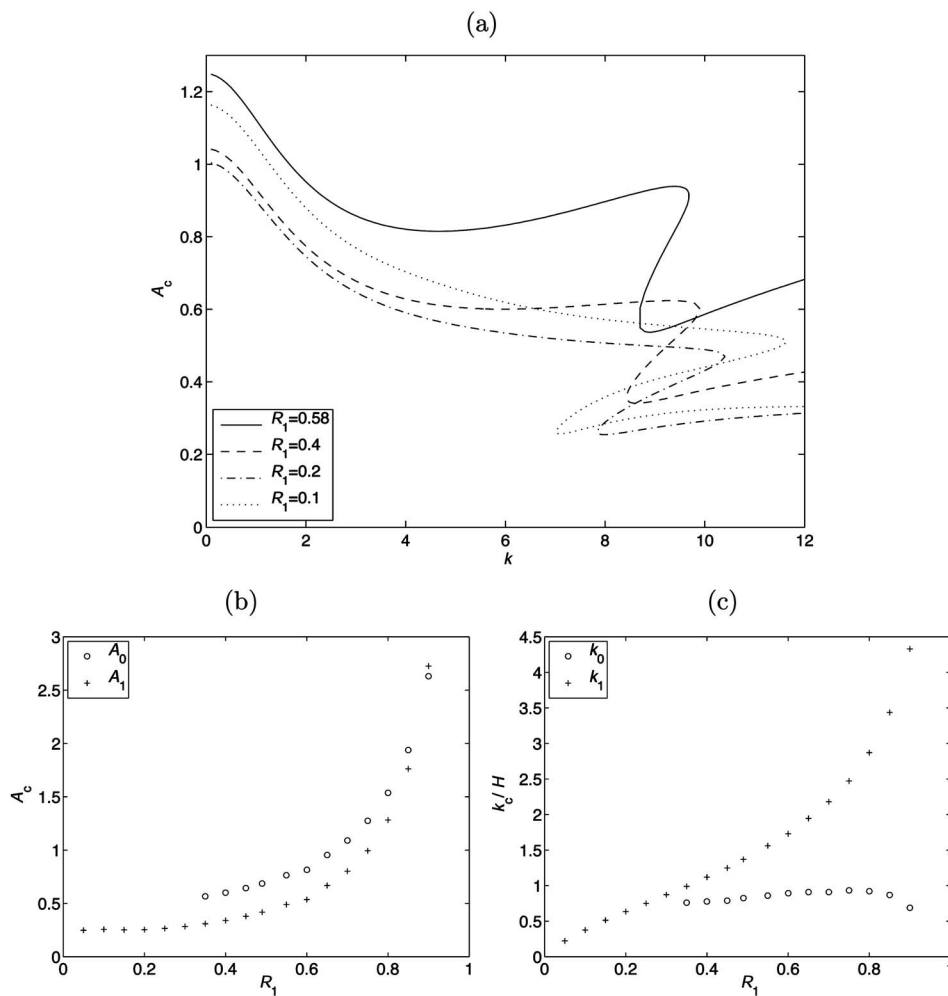


FIG. 10. (a) Neutral curves (A_c, k) for $R_1=0.58, 0.4, 0.2,$ and 0.1 . (b) Dependence of the critical amplitude of the modes k_0 and k_1 on the density contrast. (c) Dependence of k_0 and k_1 on the density contrast. The other parameter values are $\widehat{We}=2.0 \times 10^2$, $N_1=10^2$, $G_0=1.99 \times 10^{-1}$, $\Omega=1.57 \times 10^2$, and $d=1.0$.

stabilized, but also that it vanishes beyond $N_1=750$. The threshold of the k_0 mode, however, decreases as the viscosity contrast is raised. A more detailed picture of these dynamics is presented in Figs. 11(b) and 11(c), where the critical amplitudes and wavenumbers of the modes k_0 and k_1 are plotted against N_1 . In fact, A_0 exhibits a nonmonotonic dependence on N_1 with four regions of distinct dynamics similar to those uncovered by Talib *et al.*⁵ The flow becomes successively more stable, unstable and stable again as N_1 is increased, and the four regions of distinct dynamics are reflected in the variation of the critical wavenumber of k_0 with N_1 . The k_0 mode is only weakly sensitive to variations in the viscosity contrast for values of $N_1 \lesssim 10^2$, while for $10^2 \lesssim N_1 \lesssim 10^4$ its threshold decreases sharply. By contrast, the k_1 mode is strongly damped when increasing N_1 within the interval $1 \leq N_1 \leq 5 \times 10^2$. It is then destabilized within $5 \times 10^2 < N_1 < 7.5 \times 10^2$ and vanishes beyond $N_1=750$. Thus, the mode of instability at onset is k_1 up to $N_1 \approx 3.25 \times 10^2$, and k_0 beyond this value [see Fig. 11(b)]. Note that the wavenumber of k_1 varies significantly more than that of the mode k_0 , which remains close to the capillary wavenumber H .

The nonmonotonic dependence of the onset of instabilities cannot be correlated to simple features of the base flow profiles shown in Fig. 2. In these, the thickness of the interfacial boundary layer remains approximately constant in the

lower layer since $\Omega_1 = \Omega N_1$ is constant, while it increases monotonically in the upper layer with the reduction in $\Omega_2 = \Omega$. In order to gain insight into the opposite variations of the instability thresholds with increasing viscosity contrast, it is useful to examine the unstable eigenmodes. The time-averaged perturbation stream functions of the marginally unstable modes k_0 and k_1 are shown in Fig. 12 for increasing values of N_1 . We choose to represent them for $-0.04 < z < 0.04$ since the modes of instability are interfacial. The peaks in the perturbation stream functions indicate the presence of vortices, which are counter-rotating if the peaks are of opposite sign. This is illustrated in Fig. 13, where contour plots of the data shown in Fig. 12(a) are shown over one wavelength of the instability. Dark (light) shades correspond to negative (positive) values of the stream function respectively, while the medium gray horizontal and vertical lines indicate the locations where the stream function is equal to zero. In the case of the mode k_1 [Fig. 12(a) and Fig. 13], there are counter-rotating vortices present on either side of the interface, which is located at $z=0$. In the lower layer ($z < 0$), the amplitude of the stream function peak hardly changes with N_1 . In the upper layer ($z > 0$), however, the initially small stream function peak increases by a factor of approximately 2.5 for $10 \leq N_1 \leq 400$ to reach values of simi-

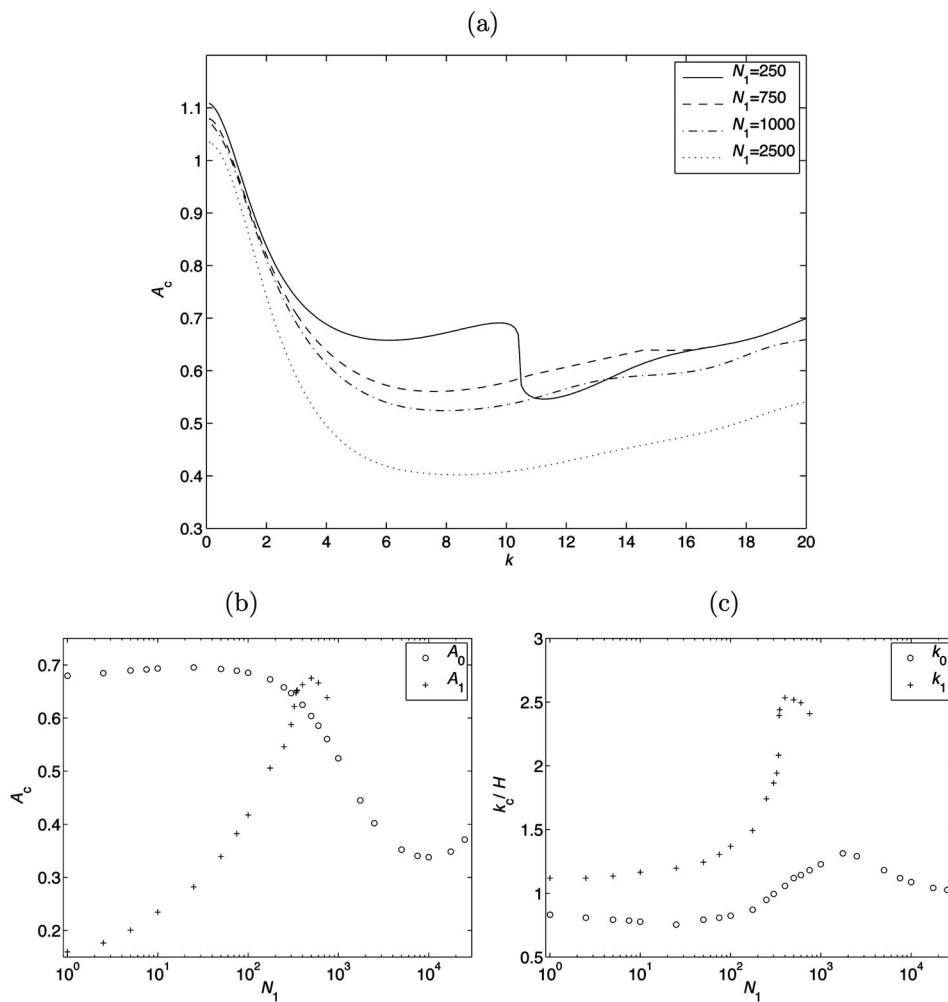


FIG. 11. (a) Neutral curves (A_c, k) for $(N_1=2.5 \times 10^2, \Omega=1.57 \times 10^2)$, $(7.5 \times 10^2, 5.24 \times 10^1)$, $(1.0 \times 10^3, 3.93 \times 10^1)$, and $(2.5 \times 10^3, 1.57 \times 10^1)$. These successive parameter values are obtained by increasing the viscosity of the upper layer, and thus raising the viscosity contrast. (b) Dependence of the critical amplitudes of the modes k_0 and k_1 on the viscosity contrast. (c) Dependence of k_0 and k_1 on the viscosity contrast. The other parameter values are $R_1=4.90 \times 10^{-1}$, $\widehat{We}=2 \times 10^2$, $G_0=1.99 \times 10^{-1}$, and $d=1.0$.

lar magnitude to those in the lower layer. As a result, the net deformation of the interface is sharply reduced, since the deformation resulting from the presence of the lower vortex is increasingly cancelled by that of the upper one, which is counter-rotating. The sharp increase in the critical wavenumber with N_1 appears to be governed by the thickness of the lower layer vortex, which becomes increasingly localized near the interface as N_1 increases from $N_1=10$ to $N_1=400$ (see Fig. 13). The concentration of vorticity near the interface in the lower layer is accompanied by the emergence of a

secondary vortex which is visible for $N_1=400$ in Fig. 13. Thus, as the viscosity ratio is increased to $N_1=400$, the stream function of the k_1 mode shown in Fig. 12(a) smoothly changes to resemble that of the k_0 mode shown in Fig. 12(b).

Indeed, the perturbation stream function of the k_0 mode [Fig. 12(b)] comprises diffuse co-rotating vortices in both layers, separated by a concentrated counter-rotating vortex right below the interface. We do not show the streamline representation in this case, as it is not well suited to visualize changes in the very thin interfacial vortex present near the

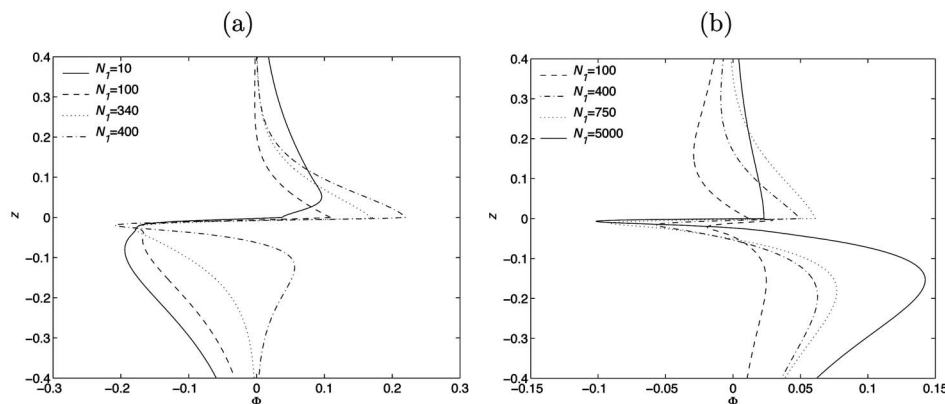


FIG. 12. Time-averaged perturbation stream functions in the vicinity of the interface (plotted for $0.4 \leq z \leq 0.4$): (a) k_1 mode with $N_1=10, 100, 340$, and 400 ; (b) k_0 mode with $N_1=100, 400, 7500$, and 5000 .

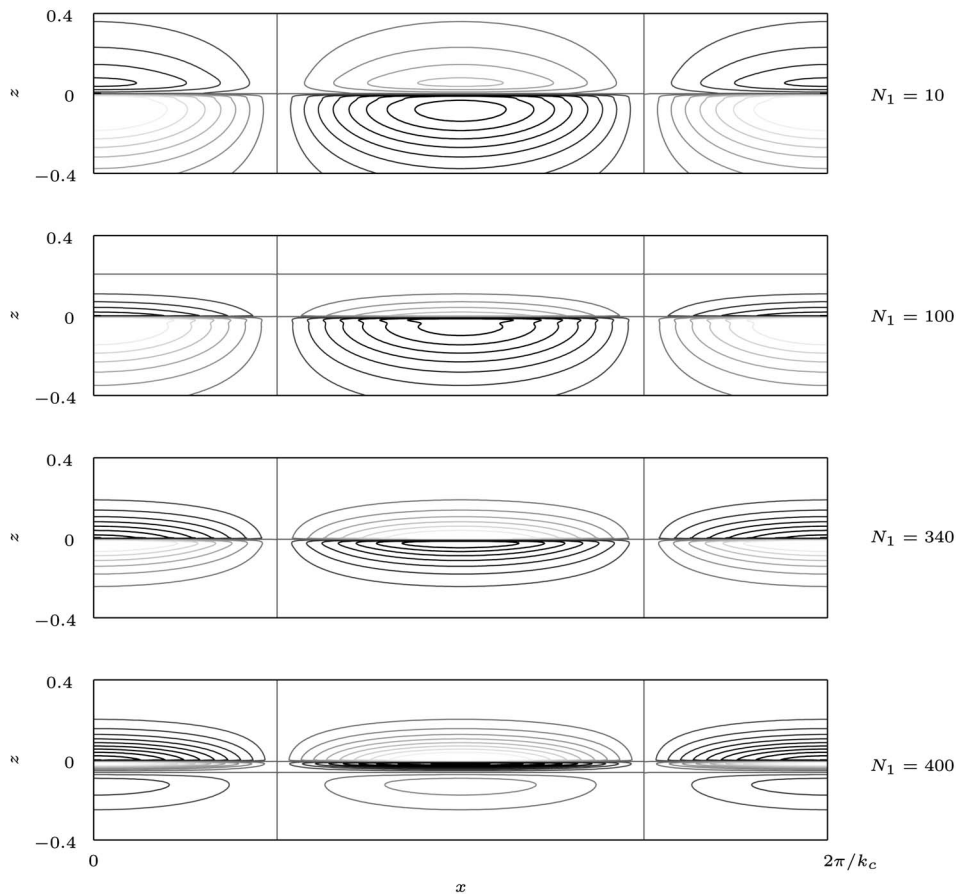


FIG. 13. Normalized streamline contour plots (over one wavelength $2\pi/k_c$), calculated using the data shown in Fig. 12(a). Dark (light) gray shades denote negative (positive) values, respectively, while the horizontal and vertical (medium gray) lines indicate where the stream function is equal to zero. Thus, these plots indicate the presence of counter-rotating vortices on either side of the interface, which is located at $z=0$. Their most striking feature is the narrowing of the lower layer vortex near the interface as N_1 increases, which correlates with the sharp rise in the wavenumber seen in Fig. 11(c).

interface in the lower layer. The considerable growth of the stream function peak corresponding to this lower layer vortex with N_1 for $10^2 < N_1 < 7.5 \times 10^2$ leads to a significant increase of the difference in magnitude of the disturbances on either side of the interface. Thus, the net deformation of the interface is sharply increased. For $N_1 = 5 \times 10^3$, the flow has entered a different regime whereby the lower layer perturbation remains unchanged but the upper layer perturbation is reduced. This yields a continued increase of the difference in magnitude of the disturbances on either side of the interface. Thus, the threshold of the k_0 instability continues to exhibit a sharp reduction with increasing N_1 . The dependence of the k_0 mode on the viscosity contrast discussed here is analogous to that of the frozen wave instability investigated by Talib *et al.*⁵ and we refer to their paper for a comprehensive discussion.

V. CONCLUSION

Horizontally oscillating viscous interfaces can be linearly unstable to a Kelvin–Helmholtz mode and successive parametric-resonance modes. The viscous model is essential to predict the onset of each mode of instability accurately, particularly in the limit of large viscosity contrasts. Since the large number of nondimensional groups prohibits an exhaus-

sive investigation of the linear solution classes, we have focused on characterizing the evolution of the neutral curves from exhibiting multiple resonances to only a single minimum, as found in the limit of practical flows. When \widehat{We} is increased toward experimental values, the first resonant mode is found to persist, rather than the Kelvin–Helmholtz mode usually associated with the frozen wave observed experimentally. Depending on the value of the density contrast R_1 , either the Kelvin–Helmholtz or the first resonant mode may be the most unstable, and similar critical parameters in the limit of small density contrasts suggest the possibility of nonlinear mode interaction. Interestingly, the two modes exhibit opposite dependencies on the viscosity contrast with a sharp stabilization of the first resonant mode, while the threshold of the Kelvin–Helmholtz mode exhibits a sharp reduction, analogously to the frozen wave instability discussed in Ref. 5.

ACKNOWLEDGMENTS

The authors wish to thank Dr W. Y. Jiang and Dr S. P. Lin for their help with the numerical method. This work was funded by an EPSRC project studentship (E. T.) and an EPSRC “Advanced Research Fellowship” (A. J.).

APPENDIX: INTEGRATION CONSTANTS OF THE BASE FLOW SOLUTION

The integration constants A_1 , B_1 , A_2 , B_2 , and S of the base flow solution, determined by substitution of the base flow solution into the boundary conditions, take the following form:

$$A_1 = -i \left(\frac{SR_1}{\Omega} - 1 \right) e^{m_1 d} - B_1 e^{2m_1 d},$$

$$A_2 = -i \left(\frac{S}{\Omega} - 1 \right) e^{-m_2} - B_2 e^{-2m_2},$$

$$B_1 = \frac{B_2(1 - e^{-2m_2}) + i(e^{-m_2} - e^{m_1 d}) + \frac{iSR_1}{\Omega}(e^{m_1 d} - 1) - \frac{iS}{\Omega}(e^{-m_2} - 1)}{(1 - e^{2m_1 d})},$$

$$B_2 = \left\{ S \left[\frac{2i}{\Omega} m_1 R_1 e^{m_1 d} - \frac{i}{\Omega} m_1 R_1 (1 + e^{2m_1 d}) - \frac{i}{\Omega} m_1 (e^{-m_2} - 1)(1 + e^{2m_1 d}) - \frac{i}{\Omega} NRm_2 e^{-m_2} (1 - e^{2m_1 d}) \right] + [iNRm_2 e^{-m_2} (1 - e^{2m_1 d}) + im_1 e^{-m_2} (1 + e^{2m_1 d}) - 2e^{m_1 d}] \right\} \times \left\{ [NRm_2 (1 + e^{-2m_2})(1 - e^{2m_1 d}) - m_1 (1 + e^{2m_1 d})(1 - e^{-2m_2})] \right\}^{-1} = \frac{SE + F}{D},$$

where \mathbf{E} , \mathbf{F} , and \mathbf{D} correspond to the terms in the three square brackets,

$$S = \left(2im_1 m_2 - im_2 (e^{m_1 d} - 1) - im_1 (1 - e^{-m_2}) + im_2 \mathbf{H} (e^{-m_2} - e^{m_1 d}) - \frac{\mathbf{GF}}{\mathbf{D}} \right) \times \left(\frac{i}{\Omega} m_1 m_2 (R_1 + 1) - \frac{i}{\Omega} m_1 (1 - e^{-m_2}) - \frac{i}{\Omega} m_2 R_1 (e^{m_1 d} - 1) + \frac{i}{\Omega} m_2 \mathbf{H} (R_1 (1 - e^{m_1 d}) + (e^{-m_2} - 1)) + \frac{\mathbf{GE}}{\mathbf{D}} \right)^{-1},$$

where

$$\mathbf{G} = m_1 (1 - e^{-m_2})^2 - \frac{m_2 (1 - e^{m_1 d})^2 (1 - e^{-2m_2})}{(1 - e^{2m_1 d})},$$

and

$$\mathbf{H} = \frac{(1 - e^{m_1 d})^2}{(1 - e^{2m_1 d})}.$$

¹K. Kumar and L. S. Tuckerman, "Parametric instability of the interface between two fluids," *J. Fluid Mech.* **279**, 49 (1994).

²G. H. Wolf, "Dynamic stabilization of the interchange instability of a liquid-gas interface," *Phys. Rev. Lett.* **24**, 444 (1970).

³S. P. Lin, J. N. Chen, and D. R. Woods, "Suppression of instability in a liquid film flow," *Phys. Fluids* **8**, 3247 (1996).

⁴A. V. Coward and D. T. Papageorgiou, "Stability of oscillatory two-phase Couette flow," *IMA J. Appl. Math.* **53**, 75 (1994).

⁵E. Talib, S. V. Jalikop, and A. Juel, "The influence of viscosity on the frozen wave instability: theory and experiment," *J. Fluid Mech.* **584**, 45 (2007).

⁶C. K. Shyh and B. R. Munson, "Interfacial instability of an oscillating shear layer," *J. Fluids Eng.* **108**, 89 (1986).

⁷H. Yoshikawa, "Instabilités des interfaces sous oscillations," Ph.D. thesis, Université Paris VI (2006).

⁸G. H. Wolf, "The dynamic stabilization of the Rayleigh–Taylor instability and the corresponding dynamic equilibrium," *Z. Phys.* **227**, 291 (1969).

⁹R. Wunnenburger, P. Evesque, C. Chabot, Y. Garrabos, S. Fauve, and D. Beysens, "Frozen wave instability by high frequency horizontal vibrations on a CO₂ liquid-gas interface near the critical point," *Phys. Rev. E* **59**,

5440 (1999).

¹⁰A. A. Ivanova, V. G. Kozlov, and P. Evesque, "Interface dynamics of immiscible fluids under horizontal vibration," *Fluid Dyn.* **36**, 362 (2001).

¹¹D. V. Lyubimov and A. A. Cherepanov, "Development of a steady relief at the interface of fluids in a vibrational field," *Fluid Dyn.* **21**, 849 (1986).

¹²S. Chandrasekhar, *Hydrodynamic and Hydromagnetic Stability* (Oxford University Press, Oxford, 1961).

¹³M. V. Khenner, D. V. Lyubimov, T. S. Belozerova, and B. Roux, "Stability of plane-parallel vibrational flow in a two-layer system," *Eur. J. Mech. B/Fluids* **18**, 1085 (1999).

¹⁴R. E. Kelly, "The stability of an unsteady Kelvin–Helmholtz flow," *J. Fluid Mech.* **22**, 547 (1965).

¹⁵M. Kamachi and H. Honji, "The instability of viscous two-layer oscillatory flows," *J. Oceanogr. Soc. Jpn.* **38**, 346 (1982).

¹⁶A. C. Or, "Finite wavelength instability in a horizontal liquid layer on an oscillating plane," *J. Fluid Mech.* **335**, 213 (1997).

¹⁷A. A. Golovin, A. A. Nepomnyashchy, and L. M. Pismen, "Interaction between short-scale Marangoni convection and long-scale deformational instability," *Phys. Fluids* **6**, 34 (1994).

¹⁸S. J. VanHook, M. F. Schatz, W. D. McCormick, J. B. Swift, and H. L. Swinney, "Long-Wavelength Instability in Surface-Tension-Driven Bénard Convection," *Phys. Rev. Lett.* **75**, 4397 (1995).

¹⁹T. I. Hesla, F. R. Pranch, and L. Preziosi, "Squire's theorem for two stratified fluids," *Phys. Fluids* **29**, 2808 (1986).

²⁰P. G. Drazin and W. H. Reid, *Hydrodynamic Stability* (Cambridge University Press, Cambridge, 1981).

²¹C. Lanczos, *Applied Analysis* (Prentice-Hall, Englewood Cliffs, 1956).

²²A. H. Nayfeh and D. T. Mook, *Nonlinear Oscillations* (Wiley, New York, 1979).

²³T. P. Schulze, "A note on subharmonic instabilities," *Phys. Fluids* **11**, 3573 (1999).